JOURNAL OF COMPUTATIONAL PHYSICS 75, 469–492 (1988)

The Ringing Instability in Particle-in-Cell Calculations of Low-Speed Flow

J. U. BRACKBILL*

Los Alamos National Laboratory, Los Alamos, New Mexico 87545

Received April 30, 1986; revised May 15, 1987

The cause of the ringing instability in particle-in-cell (PIC) fluid calculations is identified, and its properties are studied. The ringing instability is caused by aliasing, just as is the finite grid instability previously identified in PIC plasma simulation, and results in large amplitude fluctuations in the particle density. The instability occurs when the flow speed drops below a critical value, which is lower with higher order interpolation and zero with Gaussian interpolation. The instability growth rate is only weakly dependent on the number of particles per cell, but appears to be suppressed by implicit differencing in time.

INTRODUCTION

In particle-in-cell (PIC) calculations of compressible fluid flow [1], an unusual instability is sometimes observed. For example, as in the results shown in Figs. 1–4 generated with the VALLE code, large amplitude modulation of the flow variables occurs with no obvious, physical cause when the flow speed is smaller than the sound speed. The modulation, which has been called the ringing instability, is especially evident in plots depicting the particle positions, as shown.

The modulation illustrated in Figs. 1–4 has been identified previously with a linear instability due to finite differencing in time [2]. The explicit equations used in VALLE are certainly unstable, but the diffusion due to numerical errors in calculating convection stabilizes them, except where the flow stagnates. In regions of stagnation, the instability grows unimpeded. The amplitude of the resulting modulations is bounded by the limited dynamic range of the particles, and the energy is concentrated in a few modes.

More recent investigations with PIC, especially with FLIP [3], indicate that the ringing instability is more complex than can be accounted for by a finite time step instability alone. Most importantly, with an explicit, but stable, discretization in time [3] the instability is observed in regions where the flow speed is low. Further, although FLIP can be made to have a negligible amount of dissipation, the

0021-9991/88 $3.00

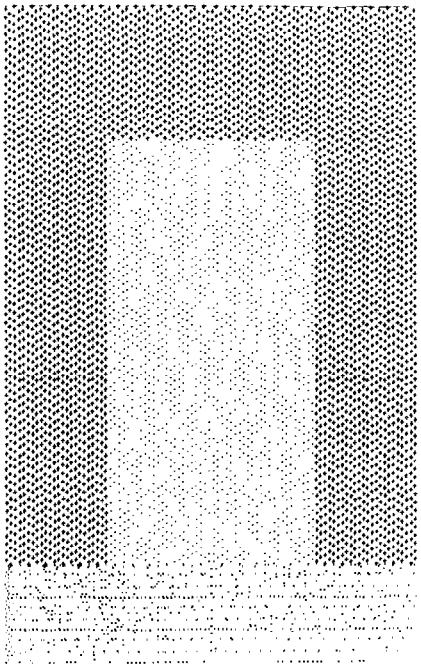

FIG. 1. Results of PIC calculations of a shock penetrating a low density, notched region by A. A. Amsden, Los Alamos Scientific Laboratory, 1967, are shown. The shock, represented by closely spaced dots, is entering the notch from below.

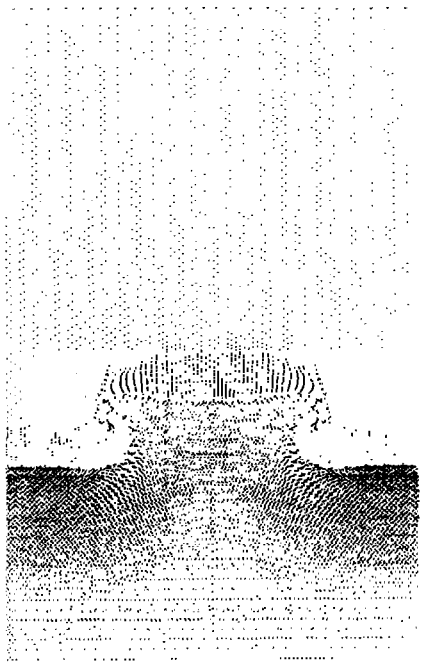

FIG. 2. As the shock propagates into the notch, interaction with the walls generates a boundary layer.

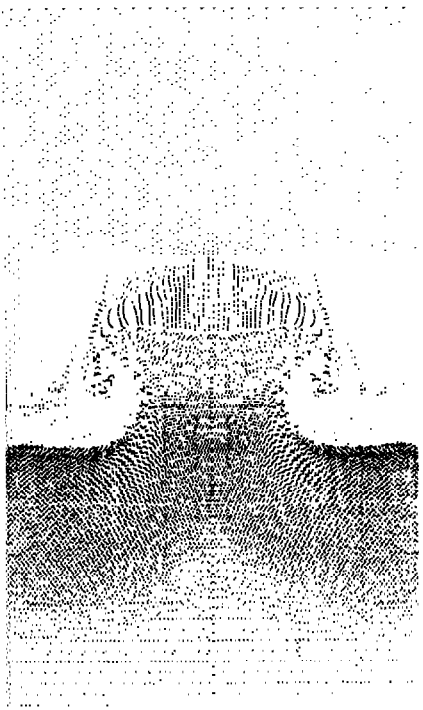

FIG. 3. The characteristic modulation of the particle density due to the ringing instability is visible in the boundary layer below the notch.

instability is not observed when the flow speed is high. Some other source for the instability must be sought than unstable differencing in time.

An alternative cause for the instability is the extensively studied, finite-grid instability which occurs in plasma simulations using PIC [4, 5]. As Dawson describes it [6], the finite grid instability has its origin "in a kind of stroboscopic effect," the same kind of effect that causes spoked wagon wheels in western movies to appear to be rotating backwards.

In PIC plasma simulations, the interactions among particles are calculated on a grid. Since all modulations of the particle density which have the same amplitudes at the grid points will produce the same interaction, two different modulations of the particle density with wavelengths that differ only by harmonics of the grid wave number, $k_g = \pi/\Delta x$ (where Δx is the mesh spacing), are indistinguishable on the grid. They are called aliases. The aliases introduce additional resonances into the dispersion relation, which may cause instability through a nonlinear interaction.

In PIC calculations of compressible fluid flows, the interactions among particles are also calculated on a grid, and aliases also occur. A calculation of the dispersion indicates that a finite grid instability occurs at low flow speeds where it is the principal component of the ringing instability. It does not occur at all at high flow

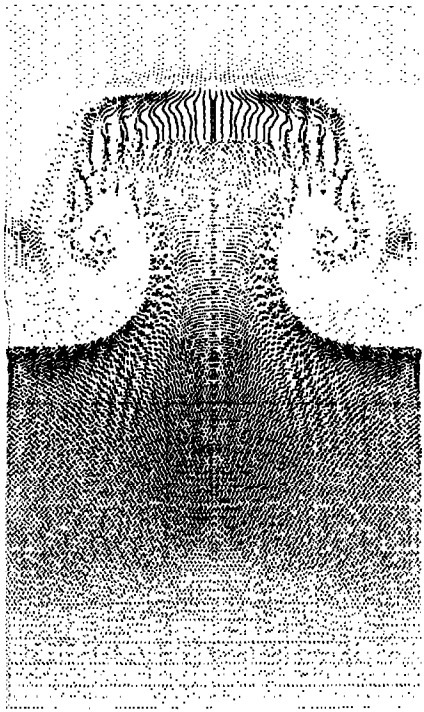

FIG. 4. The modulation of the particle density due to the ringing instability saturates when minimum density regions are devoid of particles.

speeds relative to some threshold value which depends on the particle shape function. The growth rate is finite for infinitessimal time steps.

To substantiate these observations, the dispersion theory for the finite grid instability is developed and several numerical examples are presented.

THE PARTICLE-IN-CELL MODEL

For simplicity, consider compressible flow in one dimension, which is described by the continuity and momentum equations,

$$\frac{\partial \rho}{\partial t} + u\frac{\partial \rho}{\partial x} + \rho\frac{\partial u}{\partial x} = 0, \tag{1}$$

$$\rho\left[\frac{\partial u}{\partial t} + u\frac{\partial u}{\partial x}\right] + \frac{\partial p}{\partial x} = 0, \tag{2}$$

where ρ is the mass density, u the fluid velocity, and p the pressure. The equation of state is

$$p = a^2 \rho, \tag{3}$$

where a is the sound speed.

In PIC, the fluid is represented by particles whose interactions are calculated on a grid. The particles, labeled $\not{p}$, have position, mass, and velocity, $x_{\not{p}}$, $m_{\not{p}}$, and $u_{\not{p}}$. Moments, such as mass and momentum density, are calculated by convolving a shape function, S, and the particle distribution. S is a positive function with support h and normalization one. The nth velocity moment, M^n, of the particle distribution is written,

$$\rho(x, t)\, u^n(x, t) = \frac{1}{h} \sum_{\not{p}} \int dx'\, m_{\not{p}} u^n_{\not{p}} \delta(x' - x_{\not{p}}(t))\, S(x - x'). \tag{4}$$

The integral becomes a sum over particles.

In a PIC solution of the compressible flow equations, the density is calculated at the grid points, $x_{\not{j}} = \not{j}\, \Delta x$. The support, h, is set to Δx. The pressure is calculated from Eq. (3), and the Lagrangian velocity at the grid points is advanced from Eq. (2),

$$\sum_{\not{j}'} \rho_{\not{j}\not{j}'} \frac{du_{\not{j}'}}{dt} = -\frac{\partial}{\partial x} [a^2 \rho(x)]_{x = x_{\not{j}}}. \tag{5}$$

The mass matrix, $\rho_{\not{j}\not{j}'}$, is defined below. The acceleration, which is calculated at the grid points from the momentum equation, is interpolated to the particles using S,

$$\frac{du_{\not{p}}}{dt} = \sum_{\not{j}} \int dx' \frac{du(x')}{dt} \delta(x' - x_{\not{j}})\, S(x' - x_{\not{p}}). \tag{6}$$

The displacement of the particles is calculated using the center of mass velocity calculated from Eq. (4),

$$u(x_{\not{p}}) = \frac{dx_{\not{p}}}{dt} = \frac{M^1}{M^0}. \tag{7}$$

Since u is a single valued function of x, no particle overtaking or multi-streaming can occur.

The mass density and momentum changes due to particle motion approximate the solutions of Eqs. (1) and (2). For example, differentiating Eq. (4) with respect to time (with $n = 0$) yields the mass continuity equation,

$$\frac{\partial \rho}{\partial t} = -\frac{1}{h} \sum_{\not{p}} \int dx'\, m_{\not{p}} \frac{dx_{\not{p}}}{dt} \delta'(x' - x_{\not{p}})\, S(x - x') = -\frac{\partial}{\partial x} \rho u. \tag{8}$$

Similarly, differentiating Eq. (4) (with $n=1$) yields the momentum equation,

$$\frac{\partial \rho u}{\partial t} = -\frac{\partial}{\partial x}[\rho u\, u] + \frac{1}{h}\sum_{\not\mu}\int dx'\, m_{\not\mu}\frac{du_{\not\mu}}{dt}\,\delta(x'-x_{\not\mu})\,S(x-x').$$

The integral is the change in momentum due to the acceleration of the particles. This equation can be rewritten in more familiar form by substituting from Eqs. (5), (6), and (8),

$$\left[\frac{\partial u}{\partial t} + u\frac{\partial u}{\partial x}\right] = \left\langle \frac{-(\partial/\partial x)[a^2\rho]}{\rho}\right\rangle, \tag{9}$$

where $\rho_{\not j\not j'}$, the mass matrix which appeared in Eq. (5), is defined by,

$$\rho_{\not j\not j'} = \frac{1}{h}\sum_{\not\mu}\int dx'\,\delta(x'-x_{\not\mu})\,S(x_{\not j}-x')\,S(x_{\not\mu}-x_{\not j'}).$$

The brackets on the right-hand side of Eq. (9) indicate that the acceleration is evaluated at the grid points and interpolated elsewhere as in Eq. (6).

The description of the fluid given by regularizing the particle evolution equations, Eqs. (8) and (9), is recognizably an approximation to Eqs. (1) and (2). In deriving the dispersion for the PIC equations, Eqs. (8) and (9) will be used rather than the particle equations of motion directly.

The Ringing Instability

Consider an initially uniform gas with density ρ_0 and constant flow speed U_0, which is subjected to perturbations u_1 and ρ_1. To lowest order in the perturbed variables, Eqs. (8) and (9) are written

$$\frac{\partial \rho_1}{\partial t} + U_0\frac{\partial \rho_1}{\partial x} + \rho_0\frac{\partial u_1}{\partial x} = 0, \tag{10}$$

$$\rho_0\left[\frac{\partial u_1}{\partial t} + U_0\frac{\partial u_1}{\partial x}\right] + \left\langle\frac{\partial p_1}{\partial x}\right\rangle = 0, \tag{11}$$

where $p_1 = a^2\rho_1$. These equations will be analyzed in semi-discrete form.

As usual, derivatives with respect to time are approximated by finite differences. Consider the family of theta schemes parameterized by θ and φ,

$$\frac{\rho_1^1-\rho_1^0}{\Delta t} + U_0\frac{\partial \bar{\rho}_1}{\partial x} + \rho_0\frac{\partial u_1^\theta}{\partial x} = 0, \qquad 0\leqslant\theta\leqslant 1, \tag{12}$$

$$\rho_0\left[\frac{u_1^1-u_1^0}{\Delta t} + U_0\frac{\partial \bar{u}_1}{\partial x}\right] + a^2\left\langle\frac{\partial \rho_1^\phi}{\partial x}\right\rangle = 0, \qquad 0\leqslant\phi\leqslant 1, \tag{13}$$

where $u^1 = u(x, t + \Delta t)$, $u^0 = u(x, t)$, and intermediate time levels are calculated by linear interpolation,

$$\bar{u}_1 = \tfrac{1}{2}[u_1^1 + u_1^0],$$

and

$$u_1^\theta = \theta u_1^1 + (1 - \theta)\, u_1^0 = \bar{u}_1 + (\theta - \tfrac{1}{2})(u_1^1 - u_1^0), \qquad 0 \leqslant \theta \leqslant 1,$$

and likewise ρ^ϕ.

Certain choices of θ and ϕ are distinguished. For an explicit, conditionally stable Euler scheme, one chooses $\theta = 0$, $\phi = 1$ or vice versa. For the Crank–Nicholson scheme, one chooses $\theta = \frac{1}{2}$, $\phi = \frac{1}{2}$. For a semi-implicit, unconditionally stable, backward Euler scheme, one chooses $\theta = \phi = 1$. For energy conservation in the nonlinear equations, one chooses $\theta = \frac{1}{2}$. With $\theta = \frac{1}{2}$ and $\phi = 0$, the energy conserving but unconditionally unstable scheme discussed by Harlow [1] and analyzed by Daly [2] results. With $\theta = \frac{1}{2}$ and $\frac{1}{2} < \phi \leqslant 1$, energy conserving, unconditionally stable, implicit schemes with damping of unresolved modes result [3].

The pressure is computed at the grid points from Eqs. (3) and (4). The derivative of the pressure at the grid points is calculated as in Eq. (5). To represent a fluid with constant density, particles with equal mass are equally spaced. The particle displacement is calculated from Eq. (7). A time step of a PIC fluid calculation is completed by calculating the velocity at the grid points from Eq. (4) for the next time step.

One may compare this with plasma simulation using PIC, where particle displacements depend upon individual particle velocities. By contrast, in a PIC fluid calculation the particle displacements depend upon the center of mass velocity. A detailed description of a PIC algorithm of this kind is given in Ref. [3].

The Fourier transform of the convolved density defined by Eq. (4) for any k is given by

$$\langle \rho(k) \rangle = \rho(k)\, S(k). \tag{14}$$

A point Fourier transform yields $\rho(k)$,

$$\rho(k) = \sum_p \frac{m_p}{h} e^{-ikx_p}.$$

Because the number of particles is finite, the number of Fourier modes is also finite. Thus, when there are n particles in each cell, there are n times as many Fourier modes as there are grid points.

As is pointed out in Ref. [5, Chap. 8], difficulty with aliases arises when Eq. (14) is inverted to calculate $\langle \rho_p \rangle$. Aliases occur because all Fourier modes with wavelengths shorter than the grid spacing are indistinguishable at the grid points. The inverse of Eq. (14) to calculate $\langle \rho_p \rangle$ therefore includes the additional modes

contributed by the particles, each one an alias of a principal mode. The integral over all k is equivalent, because of the periodicity of $\exp(ikx_j)$ in k, to the integral,

$$\langle \rho_j \rangle = \int_{-\pi/\Delta x}^{\pi/\Delta x} \frac{dk}{2\pi} e^{ikx_j} \sum_{l=-(n-1)/2}^{(n-1)/2} \rho(k_l)\, S(k_l), \qquad k_l = k + l\left(\frac{2\pi}{\Delta x}\right).$$

The aliases of the principal wave numbers k, $-\pi/\Delta x \leqslant k \leqslant \pi/\Delta x$, are k_l with $l \neq 0$. For quantities on the grid, therefore, Eq. (14) should be replaced by,

$$\langle \rho(k) \rangle = \sum_l \rho(k_l)\, S(k_l). \tag{16}$$

All convolved terms, when evaluated at grid points, will contribute aliases in the same way as the density. For example, one notes that,

$$p(k) = a^2 S(k) \sum_l \rho(k_l)\, S(k_l). \tag{17}$$

If one assumes the time dependence,

$$u(x, t) = u(x)\, e^{-i\omega t},$$

and introduces the frequency, Ω, defined by

$$\frac{\Omega\, \Delta t}{2} = \tan\left(\frac{\omega\, \Delta t}{2}\right), \tag{18}$$

Equations (5) and (6) can be written for any mode k_q,

$$-i[\Omega - k_\varphi U_0]\, \rho(k_\varphi) + ik_\varphi \rho_0 \left[1 - i\left(\theta - \frac{1}{2}\right)\frac{\Omega\, \Delta t}{2}\right] u(k_\varphi) = 0 \tag{19}$$

$$-i\,[\Omega - k_\varphi U_0]\, \rho_0 u(k_\varphi) + ik_\varphi a^2 \left[1 - i\left(\phi - \frac{1}{2}\right)\frac{\Omega\, \Delta t}{2}\right] S(k_\varphi) \sum_l S(k_l)\, \rho(k_l) = 0. \tag{20}$$

In this form, the coupling between k_φ and k_l is clearly exhibited. Eliminating $u(k_\varphi)$ from Eqs. (19) and (20), multiplying by $S(k_\varphi)$, and summing over φ yields the dispersion relation,

$$1 - \left[1 - i\left(\theta - \frac{1}{2}\right)\frac{\Omega\, \Delta t}{2}\right]\left[1 - i\left(\phi - \frac{1}{2}\right)\frac{\Omega\, \Delta t}{2}\right] \sum_\varphi \left\{\frac{aS(k_\varphi)\, k_\varphi}{[\Omega - k_\varphi U_0]}\right\}^2 = 0. \tag{21}$$

The solutions to Eq. (21) correspond to the natural oscillations of the system. In general, Ω is complex and exponentially growing and decaying modes occur. The dispersion relation is similar to one obtained for plasma simulation in the limit $\Delta t = 0$ with $a^2 = \omega_p^2/k^2$, where ω_p is the plasma frequency (Ref. [5, Chap. 10]).

In comparison with conventional finite difference methods, whose behavior is recovered from Eq. (21) by retaining only the $\varphi = 0$ term, the dispersion for PIC

contains one or more resonances, the number depending upon the number of particles per cell. Each resonance is the result of a particle–wave interaction. For all values of φ different from zero the wave is spurious. Nevertheless, the resonances between spurious waves and particles contribute to real waves at the principal wave numbers.

How strongly the false resonances contribute depends upon the properties of S and the values of U_0. For example, when S decreases rapidly as $|k|$ increases and U_0 is large, the contribution of the aliases will be relatively small. Conversely, if S decreases slowly as $|k|$ increases and U_0 is small, the alias contributions are relatively large and may cause instability.

Zero Time Step Limit: The Effect of the Interpolation Order on the Ringing Instability

Nearest Grid Point Interpolation

A pertinent and particularly simple dispersion relation results when one uses nearest grid point interpolation (NGP). NGP is the interpolation used to project particle mass on to the grid in the VALLE code [1].

With NGP [5], S is given by

$$S(x)=\frac{1}{\Delta x}\begin{bmatrix}0 & |x|>\Delta x/2\\ 1 & |x|\leqslant \Delta x/2\end{bmatrix} \tag{22}$$

and $S(k)$ by

$$S(k)=\frac{\sin(k\,\Delta x/2)}{k\,\Delta x/2}. \tag{23}$$

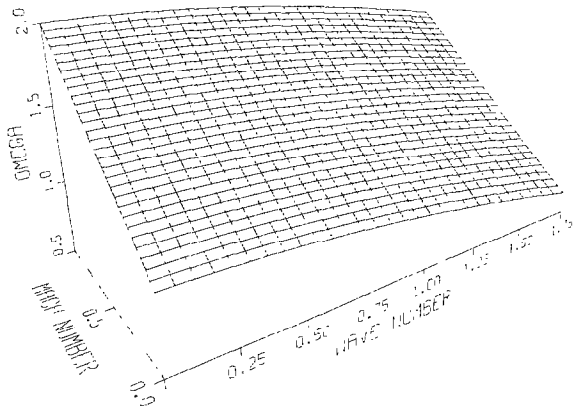

FIG. 5. The phase velocity, $\mathrm{Re}(\omega/k)$, labeled OMEGA in the figure, for NGP interpolation without aliases decreases monotonically with increasing k for all values of M.

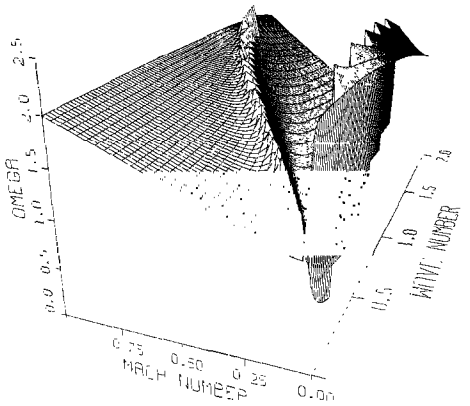

FIG. 6. The phase velocity, OMEGA, for NGP interpolation with aliases increases to a maximum value with increasing k for all $M<1$, then decreases.

With $\kappa=(\Omega/U_0-k)$, $M=U_0/a$ (Mach number), and $\theta=\phi=\frac{1}{2}$ (Crank–Nicholson scheme), summing the terms in Eq. (21) yields

$$M^2\sin^2\left[\frac{\kappa\,\Delta x}{2}\right]=\sin^2\left[\frac{k\,\Delta x}{2}\right]. \tag{24}$$

When $M^2>1$, Eq. (24) is satisfied by real values of κ for all k. However, when $M^2<1$ there are values of k for which no real solutions exist. Then, κ is complex with $\mathrm{Re}(\kappa)=\pi/\Delta x$ and $\mathrm{Im}(\kappa)$ given by

$$M^2\cosh^2\left[\frac{\mathrm{Im}(\kappa)\,\Delta x}{2}\right]=\sin^2\left[\frac{k\,\Delta x}{2}\right].$$

In Figs. 5–7, the properties of the finite grid instability with NGP are illustrated.

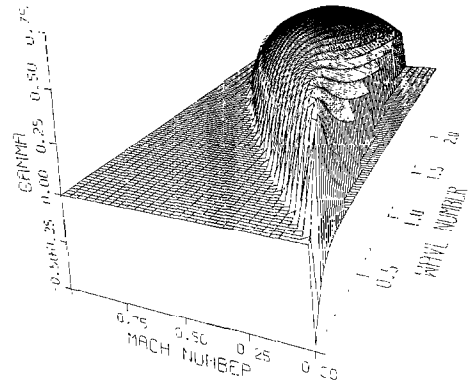

FIG. 7. The growth rate of the finite grid instability with NGP interpolation, $\mathrm{Im}(\omega/k)$ labeled GAMMA in the figure. is positive in that region of the (M,k) plane where the phase velocity is decreasing with k. Elsewhere it is zero.

In Fig. 5, $\mathrm{Re}(\omega)$ is plotted when no aliases are included and only the $\varphi = 0$ term contributes. The dispersion is exactly that which results with a stable finite difference method. The growth rate, $\mathrm{Im}(\omega/k)$, is negligible. The phase velocity, $\mathrm{Re}(\omega/k)$, decreases monotonically with increasing k, and the maximum value equal to $U_0 + a$ at $k = 0$ agrees with the analytic value. The decrease with increasing k is due to the shape function. In Fig. 6, the corresponding $\mathrm{Re}(\omega/k)$ is plotted with $-10 \leqslant \varphi \leqslant 10$ in Eq. (21). For all values of M, the phase velocity increases with k to a maximum value and then decreases. For small values of M, the wave number corresponding to the maximum phase velocity is smaller than it is at large values of M. In Fig. 7, $\mathrm{Im}(\omega/k)$ is plotted. Only $M = 0$ and $M > 1$ are stable for all values of k. For values of M between, the boundary between stable and unstable values of k coincides with the values at which $\mathrm{Re}(\omega/k)$ is a maximum. The maximum $\mathrm{Im}(\omega)$ occurs when M is about 0.3, and corresponds to a growth time equal to two oscillations at the natural frequency.

The dependence on M explains the occurrence of the instability in stagnating flow, even at zero time steps. It also accounts for the absence of the instability in high speed flow.

Higher Order Interpolation

Higher order interpolation, which means the use of higher order polynomials for S, includes several distinguishable classes of functions whose properties are different.

For example, consider the Gaussian particle shape function,

$$S(x) = \frac{1}{\pi h} e^{-x^2/2h^2}.$$

With this function and $h = \Delta x$, the ringing instability does not occur. For all values of M, the growth rate, $\mathrm{Im}(\omega)$, is essentially zero and the phase velocity, $\mathrm{Re}(\omega/k)$, looks very much like Fig. 5.

The result is of limited use, because the bandwidth of the projection operator that results from its use includes the entire grid. One must compute, or tabulate, the error function, and one loses the locality that seems appropriate for hydrodynamic flow. Nevertheless, it identifies the role of the shape function and its support in the instability.

A class of functions with compact support, which is discussed extensively by Birdsall and Langdon [5], is generated by convolving the NGP shape function with itself. These functions all reproduce a linear function exactly, and thus their projection on to the grid is calculated by evaluating the shape function at the grid vertices.

For example, linear interpolation (also called area-weighting) is defined by

$$S_1(\xi) = \frac{1}{\Delta x} \begin{bmatrix} 1 - \xi, & \xi \leqslant 1 \\ 0, & \xi > 1 \end{bmatrix}, \qquad \xi = \frac{|x|}{\Delta x}, \tag{25}$$

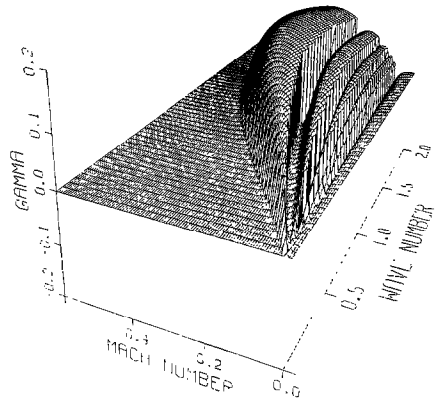

FIG. 8. The growth rate for the finite grid instability with area-weighting is shown. The portion of the (M, k) plane where the growth rate is positive is smaller, and the maximum growth rate (0.16) less than with NGP.

and can be derived from the general rule

$$S_{n+1}(x) = \int dx'\, S_n(x')\, S_0(x - x').$$

Consequently, the Fourier transform of S_n is simply

$$S_n(k) = (S_0(k))^{n+1} = \left[\frac{\sin(k\,\Delta x/2)}{k\,\Delta x/2}\right]^{n+1}.$$

The dispersion for area weighting is shown in Fig. 8. Area-weighting is more stable then NGP at all flow speeds: the critical value of M for marginal stability is about

TABLE I

The Effect of Interpolation on the Finite Grid Instability

	Maximum growth rate $(\mathrm{Im}(\omega)/ka)$		
Mach number	S^0	S^1	S^2
0.1	0.6857	0.1506	0.02739
0.2	0.6801	0.2206	0.05798
0.3	0.6691	0.2388	0.00000
0.4	0.6526	0.1768	
0.5	0.6309	0.0000	
0.6	0.6033		
0.7	0.5652		
0.8	0.4837		
0.9	0.3517		
1.0	0.2344		
1.1	0.0000		

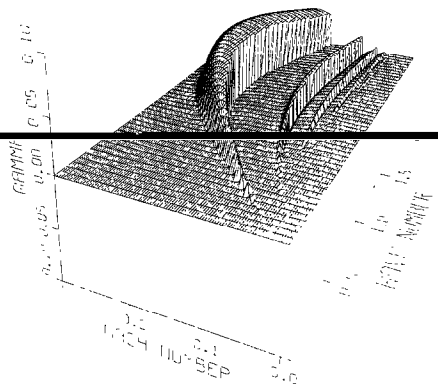

FIG. 9. The growth rate of the finite grid instability with TSC interpolation is shown. Five ridges are visible, each one associated with an alias contribution. The maximum growth rate (0.06) is one-tenth and the critical Mach number (0.2) one-fifth that with NGP.

0.4 compared with 1.0 for NGP, and the maximum growth rate is about one-third that for NGP. A comparison of the variation of the maximum growth rate with M between NGP and area-weighting is given in Table I.

With quadratic (TSC) interpolation, as shown in Fig. 9, the maximum growth rate of the ringing instability is reduced still more [7]. The interpolation function, which is written,

$$S_2(\xi) = \begin{bmatrix} \frac{3}{4} - \xi^2, & 0 \leqslant \xi \leqslant \frac{1}{2} \\ \frac{1}{2}(\frac{3}{2} - \xi)^2, & \frac{1}{2} \leqslant \xi \leqslant \frac{3}{2} \\ 0, & \xi > \frac{3}{2} \end{bmatrix} \frac{1}{\Delta x}, \qquad \xi = \frac{|x|}{\Delta x} \tag{26}$$

smooths the data. Its value, when $\xi = 0$, is $\frac{3}{4}\Delta x$ not $1/\Delta x$. The maximum growth rate of the instability is less than 0.06, about $\frac{1}{10}$ that with NGP, and the value of M for marginal stability is about 0.2. In two dimensions, the support of the interpolation function is nine grid points, compared with four for linear interpolation. The extra cost is significant, but the support for TSC is consistent with using one column or row of ghost or guard points at the edge of the mesh allowing one to impose boundary conditions similarly to NGP or area-weighting. The variation of the maximum growth rate for S_2 with M is compared with that for S_0 and S_1 in Table I.

Monaghan [7] considers another kind of interpolation function that reproduces polynomials of degree 2. The kernel, which is written,

$$W(\xi) = \begin{bmatrix} 1 - \dfrac{5\xi^2}{2} + \dfrac{3\xi^3}{2}, & 0 \leqslant \xi \leqslant 1 \\ \frac{1}{2}(2 - \xi)^2 (1 - \xi), & 1 \leqslant \xi \leqslant 2 \end{bmatrix} \frac{1}{\Delta x}, \qquad \xi = \frac{|x|}{\Delta x}$$

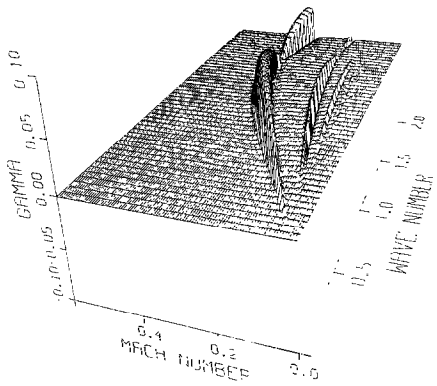

FIG. 10. The growth rate with W interpolation is positive only in several isolated ridges. Increasing the number of aliases from one to three will generate the ridges in sequence from left to right, the first alias giving the largest contribution. The maximum growth rate (0.04) is slightly less than with TSC interpolation, shown in Fig. 9, but the maximum unstable Mach number is larger.

gives ordinary, not smoothing interpolation, and its first derivative is continuous giving it similar smoothness to the quadratic interpolation function. The maximum growth rate and the region of instability, as shown in Fig. 10, are similar to S_2. However, the support is one cell larger, contributing to 25 grid points in two dimensions rather than 9 as for quadratic interpolation. Since the reduction in growth rate of the ringing instability is marginal, the increased cost discourages its use in PIC calculations.

Number of Particles

As discussed above, the number of aliases that contribute to the ringing instability increases as the number of particles per cell. If the number of aliases affects the growth rate of the instability, it is important to know how so that the correct number of particles can be used.

TABLE II

Contribution of Aliases to the Ringing Instability

	Maximum growth rate ($\mathrm{Im}(\omega)/ka$)	
Number of aliases	S^0	S^1
0	0.0000	0.0000
1	0.5522	0.2363
2	0.5982	0.2384
4	0.6298	0.2387
100	0.6691	0.2388

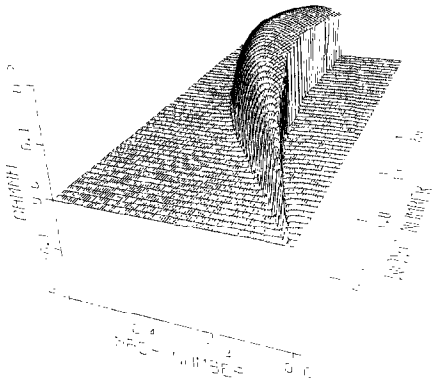

FIG. 11. With one alias, ringing produces one unstable ridge in the (M, k) plane with area-weighting interpolation. The ridge corresponds to the fastest growing mode with the maximum unstable Mach number shown in Fig. 8.

Consider the relative contribution of the φ and $\varphi + 1$ alias term in Eq. (21) with a spline interpolation function of order n. The relative contribution of the two aliases will be dominated by the dependence of the Fourier transform of S on the alias number. The ratio of sequential terms is given by

$$\frac{S_n(k_{\varphi+1})}{S_n(k_\varphi)} = \left[\frac{k\,\Delta x/2 + \varphi\pi}{k\,\Delta x/2 + (\varphi+1)\pi}\right]^{n+1}.$$

For all values of n, the ratio is smallest when $\varphi = 0$; the biggest change in the dispersion occurs when the first alias contribution is added. Further, the contributions fall off more rapidly with φ as the order of interpolation increases.

Quantitative comparisons of the dispersion with differing numbers of aliases, shown in Table II for S_0 and S_1, indicate that the relative change in the dispersion between one alias and many is modest. With NGP, the relative difference is less than 1%. With area-weighting, the corresponding difference is less than 20%.

There are qualitative changes in the dispersion with increasing number of aliases, as illustrated by a comparison of Fig. 11, with one alias, and Fig. 8, with five. Each alias adds an unstable mode with a lower growth rate and lower critical Mach number than the one before.

Evidently, increasing the number of particles is ineffectual in suppressing the ringing instability. As soon as one has particles at all, the instability may occur, and adding more will not cause it to go away.

FINITE TIME STEP: THE EFFECT OF IMPLICIT DIFFERENCING ON THE RINGING INSTABILITY

Consider the effect of a finite time step on the ringing instability. When $\theta = \frac{1}{2}$ and $\phi = 0$, the explicit, but energy conserving differencing used in VALLE is recovered.

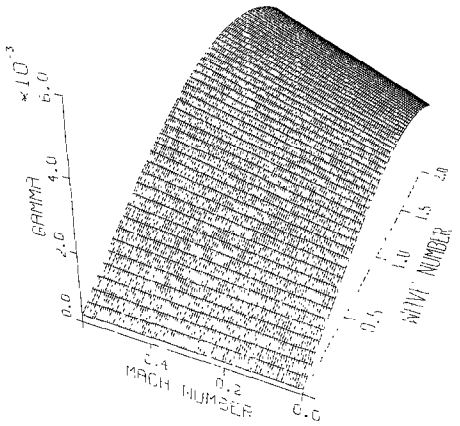

FIG. 12. With unstable, explicit time differencing ($\theta = \frac{1}{2}, \phi = 0$), a weakly growing instability occurs for all values of k and M.

Let us define, first, a stability index, C, which relates the time step, grid spacing, and flow velocity,

$$U_0 \, \Delta t = C \, \Delta x.$$

With $C = 1$ (i.e., a time step satisfying the Courant condition for stability when $\theta = 1$), the dispersion shown in Fig. 12 results with no aliases. The maximum value of $\mathrm{Im}(\omega/k)$ is similar to that with TSC, and much less than with NGP. However, the dependence on M and k is very different. There is no region of the (M, k) plane where the growth rate is zero. Instability due to a finite time step is weaker but more universal than the ringing instability.

With implicit differencing in time, $\theta + \phi > 1$, the ringing instability can be suppressed with $C \gg 1$. Consider NGP interpolation. Substituting C into the definition for κ below Eq. (23) and summing the series results in modification of the dispersion relation given in Eq. (21),

$$M^2 \sin^2\left[\frac{\Omega \, \Delta t}{2C} - \frac{k \, \Delta x}{2}\right] = \sin^2\left[\frac{k \, \Delta x}{2}\right]\left\{1 - i\left(\theta - \frac{1}{2}\right)\frac{\Omega \, \Delta t}{2}\right\}\left\{1 - i\left(\phi - \frac{1}{2}\right)\frac{\Omega \, \Delta t}{2}\right\}$$

Consider the behavior of Ω as M tends toward zero, with $(\theta - \frac{1}{2}) = (\phi - \frac{1}{2})$, and with Ω replaced by $\Omega = \Omega_0 + M\Omega_1 + \cdots$, one finds that

$$\mathrm{Im}\left\{\frac{\Omega \, \Delta t}{2}\right\} \cong -\left[\frac{1}{(\theta - \frac{1}{2})}\right]\left\{1 + M \cosh\left[\frac{1}{(\theta - \frac{1}{2})}\right]\right\}.$$

Because the assumed solution depends upon time as $\exp(-i\omega t)$, $\mathrm{Im}(\Omega) < 0$ corresponds to an exponentially decaying mode. Thus, when $\theta + \phi > 1$, the ringing modes are damped for small M where otherwise they would grow.

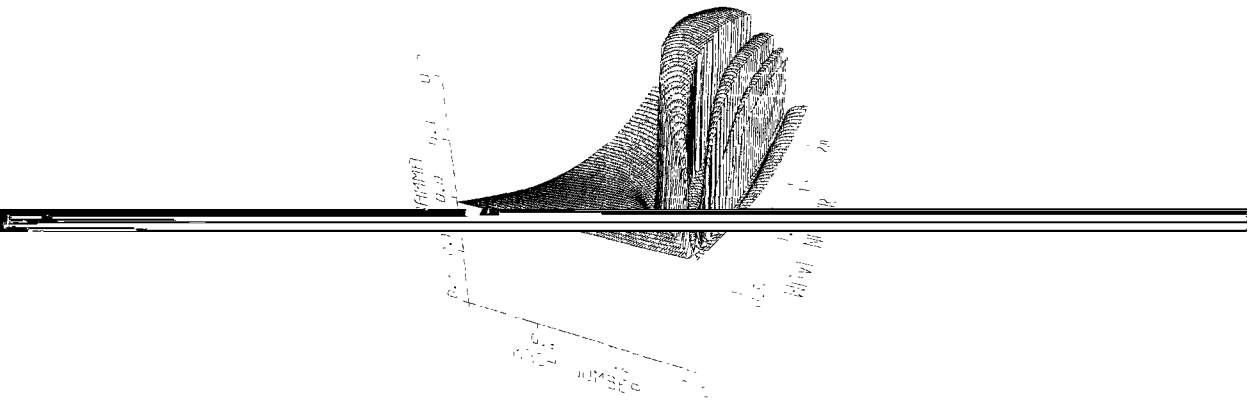

FIG. 13. With implicit, backward-Euler time differencing, damping for all values of k and M is superimposed on the ringing instability. The damping with $C = 10$ reduces the maximum growth rate by one third in comparison to Fig. 8.

This result is not unexpected when one considers the effect of very large time steps on the dynamical equations. As Hirt [8] points out, solutions with large C approach the incompressible flow limit. As is clear from the dispersion for the ringing instability, as one approaches $M = 0$, the growth rate approaches zero.

In compressible fluid flow problems, this result does not appear to be particularly useful, because to obtain stabilization, one must use a very large time step that may not resolve the time scale of interest. In Fig. 13, for example, the dispersion with area-weighting, $C = 10$, and $\theta = \phi = 1$ is similar to that shown in Fig. 8. The most evident difference is the shift downward in the basal surface due to the dissipation of the backward-Euler time differencing. The maximum growth rate and the critical Mach number are both reduced, but the modes due to the aliases are all present. To suppress the instability completely requires large values of C so that all modes with $\omega \Delta t = O(1)$ are damped, including stable, physical modes of the system. However, one might still be motivated by stability theory to use an implicit method with PIC to model problems with widely separated fast (e.g., sound waves) and slow time scales (e.g., low-speed flow). One would then choose the time step to resolve the slow scale, and not be swamped by the ringing instability.

However, the numerical results cause one to be more optimistic about the usefulness of implicit differencing than stability theory would allow. In many cases, the ringing instability is absent with implicit, and present with explicit differencing. (This may be because the approximations made in deriving Eqs. 12 and 13 are less valid as the time step increases.)

NUMERICAL EXAMPLE: HELIUM BUBBLE

The properties of the ringing instability are illustrated by a calculation of the interaction of a weak, plane shock in air with a spherical helium bubble. The

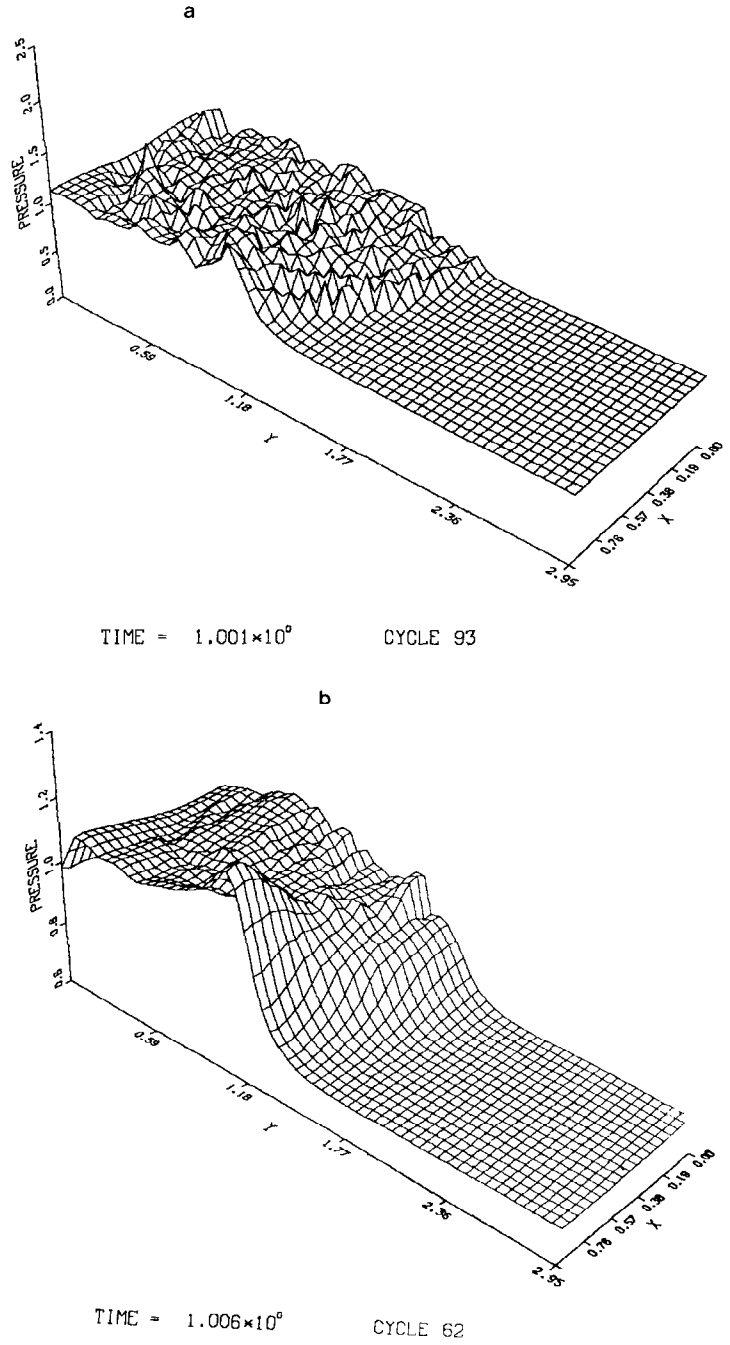

FIG. 14. The pressure variation in the calculation of the interaction of an air shock with a helium bubble depends upon the order of interpolation. As the order of interpolation increases in these explicit calculations from NGP in (a), through area-weighting in (b), to TSC in (c), the short-wavelength perturbations in pressure decrease. The shock is moving from left to right; the top boundary coincides with an axis of symmetry.

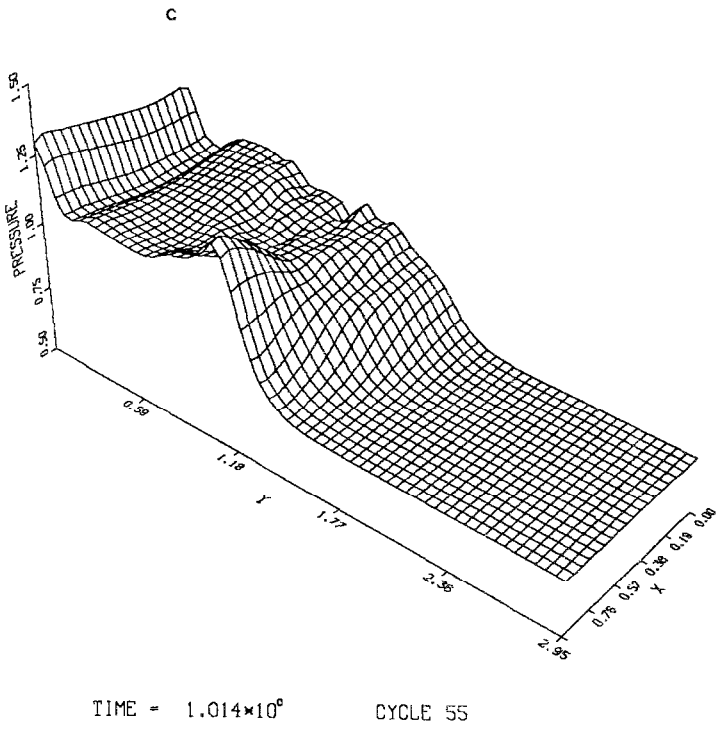

FIG. 14—*Continued.*

calculation models an experiment by Haas and Sturtevant [9], which Besnard and Haas [10] and Picone *et al.* [11] have modeled using finite difference methods. Evans *et al.* modeled similar problems with PIC [12]. The same problem is solved several different ways; with NGP, area-weighting, and TSC interpolation, and with explicit and implicit differencing in time. The occurrence and growth of the instability are shown to depend upon the order of interpolation and time-differencing as predicted by the dispersion relation.

In the problem, a spherical bubble of helium of radius R is immersed in air confined by a long, cylindrical tube of radius $2R$. A length $6R$ is included in the domain of the calculation. Time is measured in signal transit times across the cylinder radius.

The air and helium are initially in pressure equilibrium, with density ratio $\rho_{He}/\rho_{air} = 0.138$, and sound speed ratio, $a_{He}/a_{air} = 2.94$. For simplicity, both are assumed to have $\gamma = 1.4$. Air is injected into one end of the cylinder, producing a shock with strength 1.22. Air is allowed to flow out the other end as though the tube were much longer than $6R$.

The domain is resolved by a 20×60 mesh with square cells. A time step is computed each cycle that satisfies the Lagrangian flow condition,

$$\nabla \cdot u \, \Delta t > -1,$$

for implicit calculations, or the Courant condition,

$$[|u| + a]\,\Delta t < \Delta x,$$

for explicit calculations. Initially, nine particles per cell represent the fluid. Additional particles are added at one end of the tube to represent injected air.

The results for the various calculations are compared at $t = 1$. The pressures for the explicit calculations with NGP, area-weighting, and TSC interpolation are shown in Fig. 14. The figures are oriented with inflow to the left and axis of symmetry at the top. (The differences in the pressure among the cases is due to an inconsistency in the boundary data and the downstream flow conditions that causes the pressure at the boundary to oscillate in time.) The shock has progressed half the length of the mesh, and all the way across the bubble at $t = 1$. It is represented in the plots by the gentle ramp in pressure which rises from right to left.

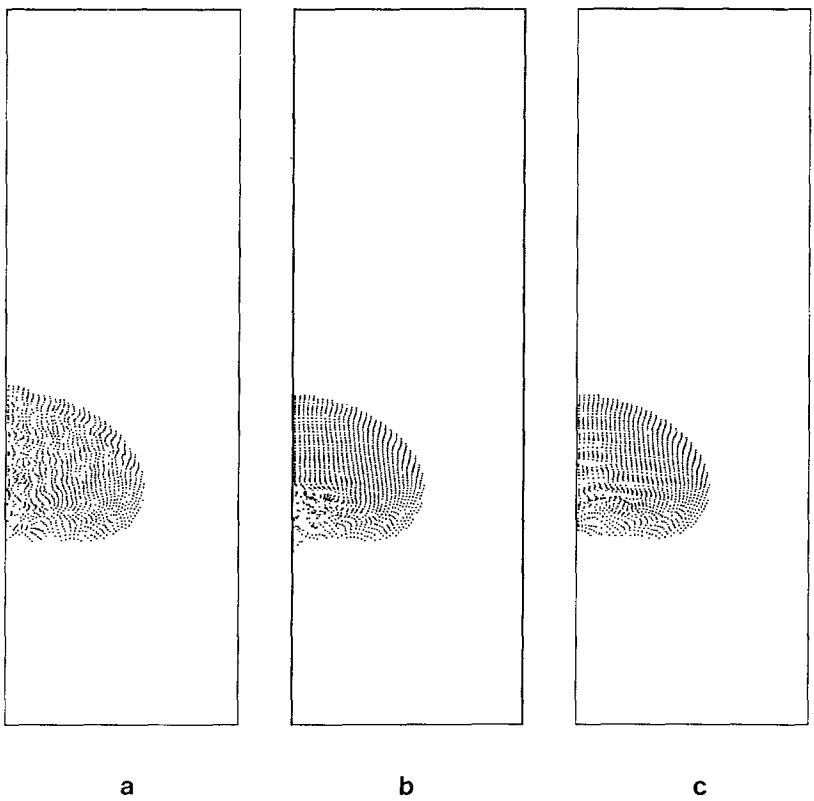

FIG. 15. The helium particles corresponding to Fig. 14 show a similar decrease in fluctuations with increasing order of interpolation. However, ringing in all cases has caused the characteristic disordering of the particles.

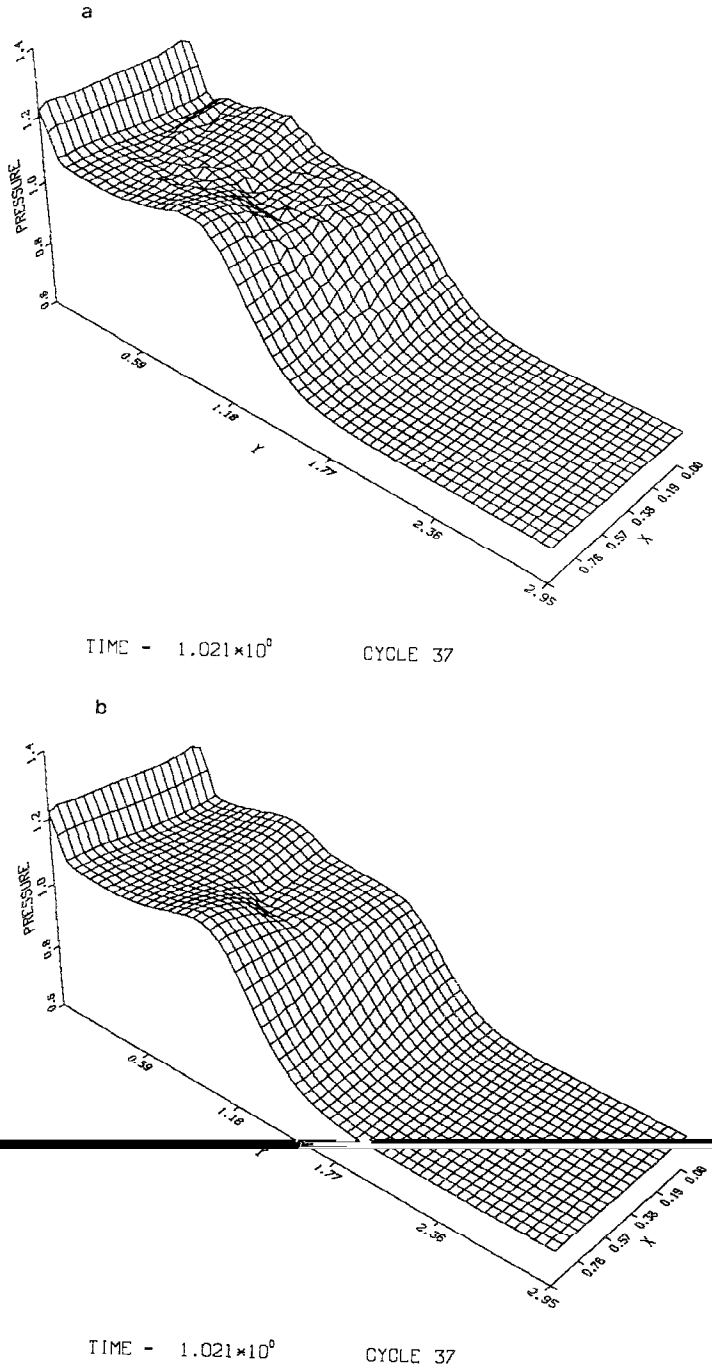

FIG. 16. Implicit time differencing gives further reductions in pressure fluctuations with area-weighting (a) and TSC (b) interpolation below the levels depicted in Fig. 14. The Courant number is about 2.

With NGP interpolation, the fluctuations in the pressure are large throughout the shocked fluids. With area-weighting, and even more with TSC, the fluctuations decrease. Evidently, the time step increases as the fluctuations decrease. With TSC interpolation, half as many cycles are needed to advance the solution the same physical time.

From other diagnostics, the flow velocity in the helium corresponds to $0.1 < M < 0.3$, and all three interpolation functions support the ringing instability. In air, however, where $M < 1$ behind the shock, only NGP is unstable. Thus, with NGP the fluctuations are large everywhere. With area-weighting, and especially with TSC, the fluctuations are confined to the helium (along the axis of symmetry, behind the shock).

The corresponding particle plots are shown in Fig. 15. Only the particles in the helium bubble are shown. The ringing instability causes a growing disordering of the initially rectilinear arrays of particles, which stops, typically, only when the particles are clumped in bands one wavelength of the unstable mode apart. At the early time shown, the disordering is distributed throughout the bubble with NGP; the disordering has progressed only to a few horizontal gaps with TSC. The growth rate is least with TSC, consistent with the dispersion derived above.

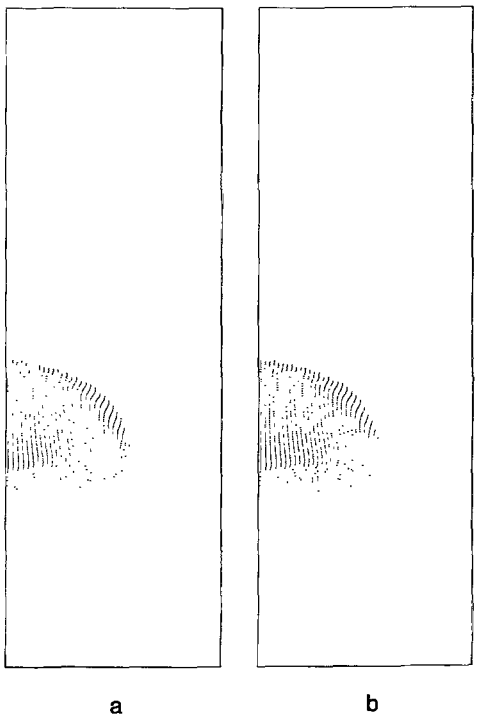

FIG. 17. The ringing instability has caused no disordering in the particles corresponding to Fig. 16 with area-weighting (a) and TSC (b) interpolation when time is differenced implicitly.

The pressures for the implicit calculations with area-weighting and TSC interpolation are shown in Fig. 16. The time step is larger than before, with $C \approx 1.8$, but not large enough to cause significant damping. Nevertheless, the implicit cases are obviously smoother than the explicit cases. In fact, in the corresponding particle plots shown in Fig. 17, the ringing instability is completely absent. The particles are beautifully ordered.

Conclusions

The investigation of the ringing instability in PIC calculations of compressible fluid flow has yielded several clear results. The finite-grid instability identified in plasma simulations also occurs in PIC fluid calculations where it is the principal contributor to the ringing instability. The strength of the ringing instability can be reduced using higher order interpolation with extended support; it can be eliminated if the support includes the entire mesh. Even with relatively low-order interpolation, the ringing instability appears not to grow with implicit differencing in time.

The ringing instability exhibits little dependence on the number of aliases. Correspondingly, there is little dependence on the number of particles per cell that are used in a calculation.

No scaling with the grid spacing is observed. However, the introduction of a dissipation length scale through a viscosity would introduce a scaling. The probable overall effect would be stabilizing.

The results of this analysis and the existence of a similar instability in plasma simulation together suggest the finite grid or ringing instability is a fundamental property of particle-in-cell codes. The large number of modes supported by the particles that are not distinguished on the grid is the source of the instability. Only measures that remove this degeneracy without introducing large dissipation will eliminate the instability without diminishing the usefulness of the PIC method.

Acknowledgments

The author is grateful to A. A. Amsden, B. J. Daly, and F. H. Harlow for the unpublished figures from VALLE calculations, and to J. J. Monaghan for helpful suggestions on the manuscript.

References

1. F. H. Harlow, "The Particle-in-Cell Method for Numerical Solution of Problems in Fluid Dynamics," *Experimental Arithmetic, High-Speed Computations and Mathematics* (Amer. Math. Soc., Providence, RI, 1963); A. A. Amsden, "The Particle-in-Cell Method for the Calculation of the Dynamics of Compressible Fluids," Los Alamos National Laboratory, LA-3466, 1966 (unpublished).
2. B. J. Daly, *Math. Comput.* **17**, 346 (1963).
3. J. U. Brackbill and H. M. Ruppel, *J. Comput. Phys.* **65**, 314 (1986).

4. A. B. LANGDON, *J. Comput. Phys.* **6**, 247 (1970); E. L. LINDMAN, *J. Comput. Phys.* **5**, 13 (1970).
5. C. K. BIRDSALL AND A. B. LANGDON, *Plasma Physics via Computer Simulation* (McGraw–Hill, New York, 1985).
6. J. DAWSON, *Rev. Mod. Phys.* **55**, 403 (1983).
7. J. J. MONAGHAN, *Comput. Phys. Rep.* **3**, 72 (1985).
8. C. W. HIRT, A. A. AMSDEN, AND J. L. COOK, *J. Comput. Phys.* **14**, 227 (1974).
9. J.-F. HAAS AND B. STURTEVANT, "Interaction of Weak Shock Waves with Cylindrical and Spherical Gas Inhomogeneities," Graduate Aeronautical Laboratory, California Institute of Technology, 1986 (unpublished).
10. D. BESNARD AND J.-F. HAAS, Centre d'Etudes de Limeil, Villeneuves, France, private communication (1986).
11. J. M. PICONE, J. P. BORIS, E. S. ORAN, AND R. AHEARNE, "Rotational Motion Generated by Shock Propagation through a Non-uniform Gas," 15th International Symposium on Shock Waves and Shock Tubes, Stanford University, CA, 1986.
12. M. W. EVANS, F. H. HARLOW, AND B. D. MEIXNER, *Phys. Fluids* **5**, 651 (1962).